

# A Hybrid Multi-Path CMOS Magnetic Sensor With 76 ppm/°C Sensitivity Drift and Discrete-Time Ripple Reduction Loops

Junfeng Jiang and Kofi A. A. Makinwa, *Fellow, IEEE*

**Abstract**—This paper presents a temperature-insensitive magnetic sensor system for contactless current measurements. To simultaneously achieve wide bandwidth and low noise, the proposed system employs a multi-path structure with a set of spinning current Hall sensors in its low-frequency path and a set of pick-up coils in its high-frequency path. The Hall sensors and pick-up coils are used in a differential sensing arrangement that naturally rejects common-mode magnetic field interference, e.g., due to the earth's magnetic field. A common-mode ac reference field can then be used to continuously stabilize the sensitivity of the Hall sensors, which, unlike that of the pick-up coils, is quite temperature dependent. In this design, the ripple reduction loops in the Hall sensor readout are implemented in a discrete-time manner, and so occupy 20% less area than a previous continuous-time implementation. Over a  $-45^{\circ}\text{C}$  to  $105^{\circ}\text{C}$  temperature range, the proposed system reduces the Hall sensor drift from 22% to 1%, which corresponds to a temperature coefficient of 76 ppm/°C.

**Index Terms**—Discrete-time, Hall sensor, low drift, magnetic sensor, pick-up coils, ripple reduction loops, sensitivity stabilization, wide bandwidth.

## I. INTRODUCTION

MAGNETIC sensors are widely used in many applications for control, protection, and diagnostic purposes. In low-power applications such as consumer electronics, current sensing is usually done using shunt resistors for high accuracy [1]. However, in high-voltage and high-power environments such as in industrial and automotive applications, galvanic isolation is required, which complicates the use of shunt-based current sensors. Instead, magnetic sensors can be used to indirectly sense current by sensing the associated magnetic field. This approach also offers more flexibility, allowing systems to be retrofitted without breaking existing current traces [2].

Present industrial trends toward higher efficiency and lower cost have led to the use of compact switched-mode power supplies based on small inductors, which must then be operated at

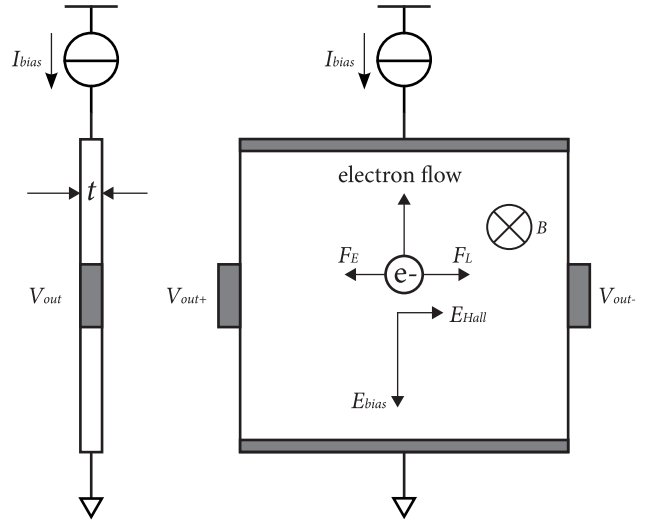


Fig. 1. Side (left) and top (right) views of a Hall effect sensor.

higher frequencies [3]. State-of-the-art switched-mode power supplies typically operate at frequencies well above 1 MHz [4]. In order to measure the currents in such systems, sensors with wide bandwidth, e.g.,  $>1$  MHz, are required. Such sensors are also required in overload or short-circuit protection modules [5], [6] to ensure that fault currents are rapidly detected, e.g., within  $1\ \mu\text{s}$ , to avoid catastrophic failures.

Hall-effect sensors (Hall sensors) have found widespread applications due to their excellent linearity, CMOS compatibility, and hence low cost. In the presence of a magnetic field, electrons will experience a Lorentz force, as shown in Fig. 1. Therefore, positive and negative charges will accumulate at the terminals  $V_{\text{out}+}$  and  $V_{\text{out}-}$ , respectively. The force exerted by the resulting electric field counterbalances the Lorentz force experienced by the electrons and establishes a thermal equilibrium state [7]. The output voltage  $V_{\text{out}}$  is then proportional to the strength of the input magnetic field and to the current density ( $I_{\text{bias}}/t$ ), where  $t$  is the thickness of the sensor. The time required to establish equilibrium is related to the relaxation time of electrons, which is in the order of  $10^{-14}$  s [7]. This indicates that the Hall effect is a fast physical phenomenon, which can potentially achieve bandwidths of several gigahertz. In the 60s, in fact, they were widely used for micro-wave measurements [8].

However, in CMOS processes, Hall sensors are commonly realized as n-well plates, which usually exhibit significant offset, ranging from 10 to 50 mT [9], [10]. This is the orders of magnitude greater than many signals of interest, e.g.,

Manuscript received November 23, 2016; revised January 31, 2017; accepted March 10, 2017. Date of publication March 18, 2017; date of current version June 22, 2017. This paper was approved by Guest Editor Wim Dehaene. This work was supported by Texas Instruments and STW (Dutch Technology Foundation). (Corresponding author: Junfeng Jiang.)

J. Jiang is with the Electronic Instrumentation Laboratory, Delft University of Technology, 2628 CD Delft, The Netherlands, and also with Texas Instruments Deutschland GmbH, 85356 Freising, Germany (e-mail: j.jiang-1@tudelft.nl; j-jiang@ti.com).

K. A. A. Makinwa is with the Electronic Instrumentation Laboratory, Delft University of Technology, 2628 CD Delft, The Netherlands.

Color versions of one or more of the figures in this paper are available online at <http://ieeexplore.ieee.org>.

Digital Object Identifier 10.1109/JSSC.2017.2685462

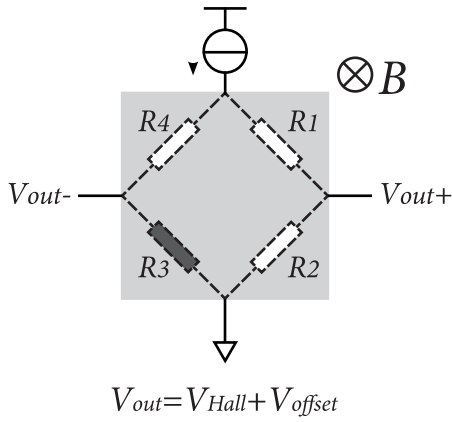


Fig. 2. Wheatstone bridge model of Hall sensors.

the earth's magnetic field, which ranges from 25 to 65  $\mu\text{T}$  [11]. The origins of this offset can be understood by regarding a Hall sensor as a Wheatstone bridge, as shown in Fig. 2, which will be unbalanced by the inevitable n-well inhomogeneity. Fortunately, as shown in Fig. 3, this offset can be suppressed with the help of the spinning current technique [12]. By periodically alternating (or spinning) the relative positions of the Hall sensor's biasing and readout terminals, magnetic signals will be up-modulated to  $f_{\text{spin}}$  and can thus be distinguished from the dc offset. A demodulator can then be used to detect the magnetic signal and simultaneously up-modulate the offset of both the sensor and its readout circuitry into ac ripple. The spinning current technique can be considered to be quite similar to chopping, and confers a similar reduction of  $1/f$  noise and drift.

Due to the n-well's anisotropic resistivity, the value of the various resistances in the Wheatstone bridge model will depend on the direction of its biasing current [13]. Furthermore, due to the voltage drop across the n-well, the thickness of the depletion region between it and the p-substrate will not be uniform. As a result, the value of the various resistances in the Wheatstone bridge model will be systematically different, with the resistances connected to ground (Fig. 3) being slightly smaller than the other two [7]. The magnitude of the offset generated in the two phases of the spinning current technique will thus vary, resulting in a net residual offset. To reduce this, the spinning current technique usually consists of four phases, which employ all four possible biasing directions of the n-well [14]. With this method, residual offsets of about 10  $\mu\text{T}$  can be achieved [14]. This can be further reduced, to 4  $\mu\text{T}$ , by applying an eight-phase spinning sequence to an octagonal n-well plate [15].

Since a Hall sensor's offset is usually much larger than the desired magnetic signal, the amplitude of the up-modulated spinning ripple is quite large, and must be reduced. Conventional approaches use low-pass filters, which also unfortunately limit the sensor's bandwidth. Increasing the spinning frequency  $f_{\text{spin}}$  can alleviate this issue, but usually results in a higher residual offset [16] due to the increased frequency of charge injection and switching transients. As a result, the bandwidth of low-offset CMOS Hall sensors is typically rather low ( $<100$  kHz) [16]. In [17], this constraint was addressed by using three orthogonal ripple reduction loops (RRLs)

to continuously measure and suppress the spinning ripple before amplification. Together with multi-path and multi-sensor techniques [18], an un-trimmed Hall sensor system achieved a 40  $\mu\text{T}$  offset and a flat bandwidth of 400 kHz. However, the RRLs in [18] were implemented in a continuous-time manner, and so occupied a relatively large chip area.

Since a Hall sensor is essentially a resistor, its SNR decreases with an increasing bandwidth. In a bid to achieve both wide bandwidth and high resolution, Hall sensors and pick-up coils were combined in a multi-path architecture [19], [20]. As shown in Fig. 4, the crossover frequency  $f_{\text{cross}}$  defines the frequency beyond which the pick-up coils, due to their superior SNR at high frequencies (HFs), should take over from the Hall sensors. As shown in Fig. 5, this is realized with the help of a transimpedance amplifier (TIA), which low-pass filters the Hall signals and integrates the coil signals. The noise bandwidth of the system is thus limited (to 2 kHz), while the coil extends the sensor's bandwidth (to 3 MHz) with, in principle, no added noise. The crossover frequency  $f_{\text{cross}}$  is set by the TIA's  $RC$  feedback network. As such, a smooth transition between the two paths is guaranteed even in the face of temperature changes and process spread. To achieve a flat bandwidth, the sensitivity of the Hall sensor is matched to that of the pick-up coil by adjusting the Hall sensor's biasing current. However, primarily due to changes in carrier concentration, the sensitivity of a Hall sensor is quite temperature dependent, and will drift more than 20% from  $-70$   $^{\circ}\text{C}$  to  $170$   $^{\circ}\text{C}$  [7]. This is in contrast to the sensitivity of the voltage-output pick-up coils, which is essentially temperature independent.

To address this problem, Hall sensor sensitivity can be adjusted using temperature information acquired by an on-chip temperature sensor. With this approach, a sensitivity drift of 30 ppm/ $^{\circ}\text{C}$  has been achieved from  $-40$   $^{\circ}\text{C}$  to  $120$   $^{\circ}\text{C}$  [21]. However, this method requires accurate characterization of both the Hall and temperature sensors over the entire temperature range, which is time consuming, and thus, costly.

Alternatively, as shown in Fig. 6, the Hall sensor's sensitivity can be continuously monitored with the help of an ac magnetic field reference generated by on-chip coils [22]. The corresponding output signal  $V_{\text{ref}}$  can then be locked to a constant set-point, which effectively stabilizes the Hall sensor's sensitivity. Without on-chip temperature sensors, a sensitivity drift of 50 ppm/ $^{\circ}\text{C}$  can be achieved [22]. However, the reference signal must be located at a frequency outside the sensor's signal bandwidth, and so this approach is impractical for wide-bandwidth designs.

To avoid a loss of bandwidth, this paper proposes a sensitivity stabilization scheme that uses a common-mode reference field generated by a set of on-chip coils. This approach exploits the fact that the differential sensor arrangement used for current measurements naturally rejects common-mode fields, thus allowing system sensitivity to be continuously monitored without interfering with differential signals. The rest of this paper is organized as follows. Details of the proposed system, including the discrete-time RRLs, are described in Section II. Measurement results are shown and discussed in Section III. This paper concludes in Section IV.

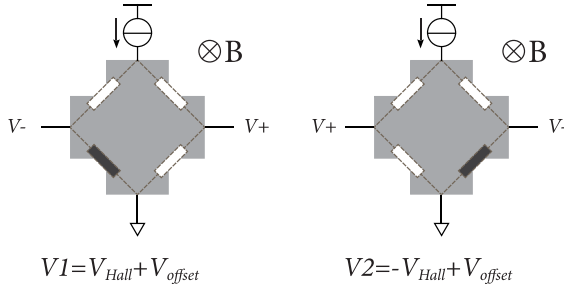


Fig. 3. Spinning current Hall sensors (left) and its readout (right).

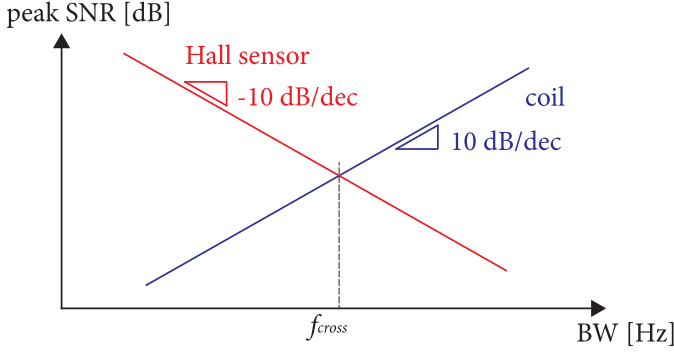


Fig. 4. Peak SNR plots of Hall sensors and coils.

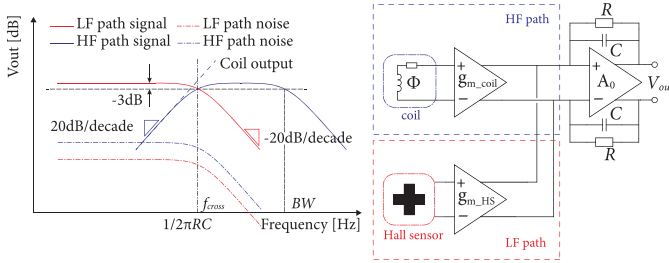


Fig. 5. Combination of Hall sensors and pick-up coils.

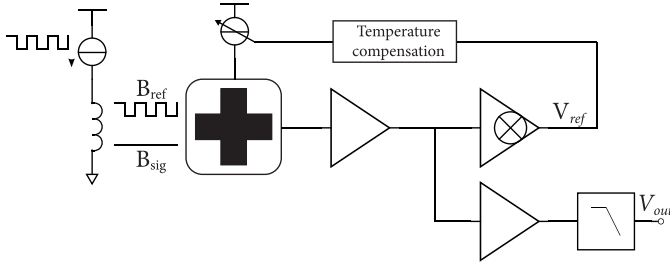


Fig. 6. Closed-loop temperature control using on-chip coils.

## II. SYSTEM IMPLEMENTATION

The proposed system is briefly illustrated in Fig. 7. A set of coils generates a common-mode ac magnetic field which is superimposed on the differential magnetic signal induced by the current flowing through a primary trace on a PCB. Both these fields are picked up by two sets of Hall sensors, and then amplified. Subtracting the amplifiers' output results in a differential channel, whose output is proportional to the differential magnetic field, and in which the contribution of the

### Spinning current Hall sensor

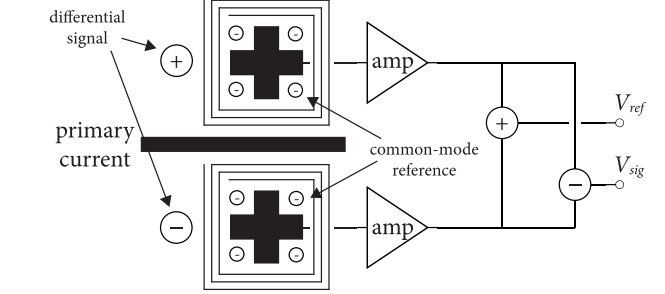
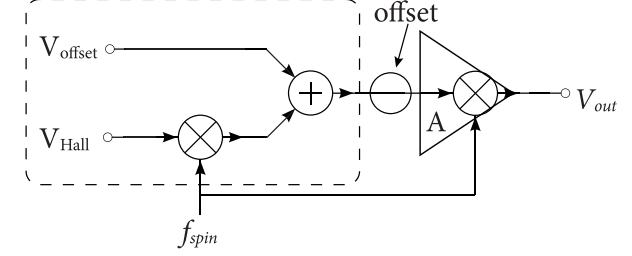


Fig. 7. Sensitivity extraction via an on-chip common-mode ac reference field.

common-mode field is canceled. Conversely, summing their outputs results in a common-mode channel, whose output is proportional to the common-mode field, and in which the contribution of the differential field is canceled. The output of the common-mode channel  $V_{ref}$  can then be used to monitor and stabilize the Hall sensor's sensitivity. The frequency of the common-mode field can now be safely located within the sensor's bandwidth, since it is strongly attenuated in the differential channel.

### A. $g_m$ -Based Hall Sensor Readout in a Hybrid Magnetic Sensor System

The block diagram of the overall system is shown in Fig. 8. It inherits the high-frequency (HF) path design from [20]. A transconductance  $g_{m\_coil}$  converts the outputs of a pick-up coil into currents, which are integrated by the TIA. To preserve the offset performance of the low-frequency (LF) path, a coupling capacitor  $C_{AC}$  is used to block the offset of  $g_{m\_coil}$ . A dc servo loop then prevents the output of  $g_{m\_coil}$  from clipping.

To minimize their initial offset, each Hall sensor in the LF path consists of four orthogonally-coupled Hall plates [23]. The spinning current technique is then used to further reduce this offset. In [19], the Hall sensors were read out by a capacitively-coupled instrumentation amplifier, which, however, required a large input capacitor to achieve low noise. In this paper, an area-efficient  $g_m$ -based readout scheme is used, since two readout channels are now required to simultaneously extract the differential and common-mode signals.

As shown in Fig. 8, the differential channel is realized by two  $g_m$  stages ( $g_{m\_HS}$ ) that convert the outputs of the two Hall sensors into currents, which are demodulated and subtracted to extract the differential signal. A TIA combines this signal with

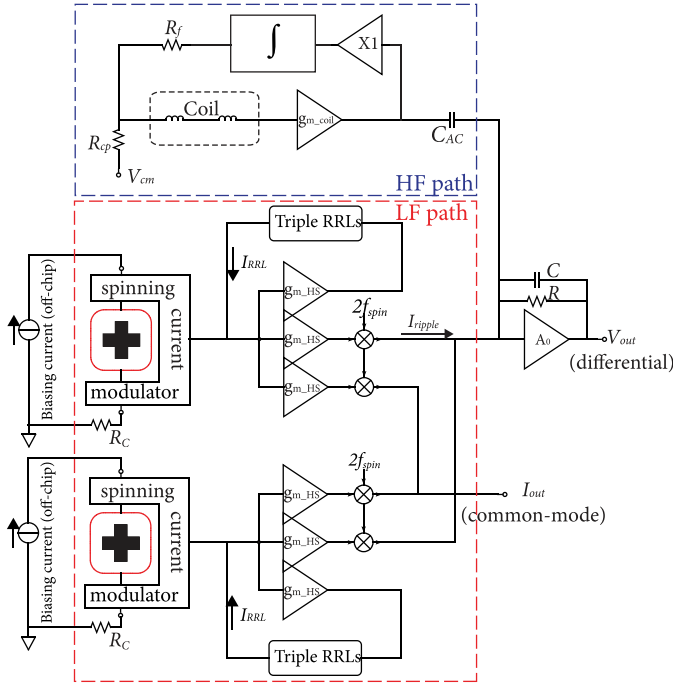
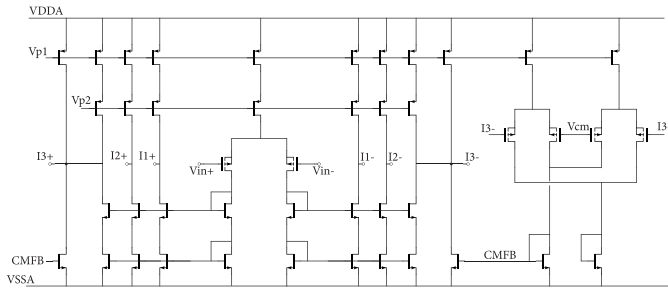


Fig. 8. Block diagram of the complete system.

Fig. 9. Circuit diagram of  $g_{m\_HS}$ .

the output of the HF path. In a similar manner, the common-mode channel is realized by summing the two  $g_{m\_HS}$  outputs. The combined sensitivity of the Hall sensors and  $g_{m\_HS}$  can be stabilized by locking this output current to a set-point. For flexibility, the temperature control loop is implemented off-chip, and is discussed in more detail in Section III.

To suppress the spinning ripple, two sets of triple RRLs feed offset compensation currents directly into the two Hall sensors. This is in contrast to [20], in which the RRL's acted on the output of a pre-amplifier. Since their offset is cancelled by the RRLs, the Hall sensors produce relatively small output signals (in the order of 100  $\mu V$ ), which greatly simplifies the design of  $g_{m\_HS}$ . The residual ripple will then be limited by the mismatch between the three  $g_{m\_HS}$  stages. To minimize this, they are implemented as a single  $g_m$  stage with three output branches, which consume a total current of about 500  $\mu A$ , as shown in Fig. 9 [24]. Each branch has its own common-mode feedback loop, only one of which is shown in Fig. 9. To match the common-mode level of the Hall sensors' outputs to that of the  $g_{m\_HS}$  input pair, a resistor  $R_C$  is inserted between the Hall sensors and ground, as shown in Fig. 8.

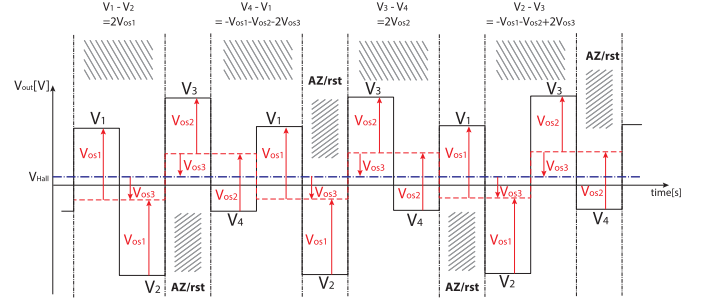


Fig. 10. Illustration of triple RRL scheme.

### B. Discrete-Time Triple RRLs

In this design, the outputs of the two Hall sensors are individually processed to simultaneously extract differential and common-mode signals. The continuous-time implementation of the triple RRLs, as in [18] and [19], would then occupy considerable chip area, mainly due to the need to realize three independent analog integrators. In this design, the integrators are implemented as up/down counters in an area-efficient discrete-time manner [25].

Fig. 10 shows the output waveform of a typical four-phase spinning-current Hall sensor. Its output during each of the four spinning phases  $V_{1-4}$  can then be expressed in terms of the magnetic signal  $V_{Hall}$  and three offset components  $V_{os1}$ ,  $V_{os2}$ , and  $V_{os3}$  as follows:

$$V_1 = V_{Hall} + V_{os1} + V_{os3} \quad (1)$$

$$V_2 = V_{Hall} - V_{os1} + V_{os3} \quad (2)$$

$$V_3 = V_{Hall} + V_{os2} - V_{os3} \quad (3)$$

$$V_4 = V_{Hall} - V_{os2} - V_{os3} \quad (4)$$

Offsets  $V_{os1}$  and  $V_{os2}$  can be directly extracted by computing  $V_1 - V_2$  and  $V_3 - V_4$ , respectively. Information about  $V_{os3}$  is, however, contained in  $V_4 - V_1$  and  $V_2 - V_3$

$$V_4 - V_1 = -V_{os1} - V_{os2} - 2V_{os3} \quad (5)$$

$$V_2 - V_3 = -V_{os1} - V_{os2} + 2V_{os3} \quad (6)$$

Equations (5) and (6) indicate that  $V_{os3}$  can be extracted from these signals, provided that  $V_{os1}$  and  $V_{os2}$  become sufficiently small, i.e., after the other RRLs have settled. This means that one of the three offset components can be extracted from the outputs of every two adjacent spinning phases, allowing the reuse of hardware and hence, saving chip area.

The implementation of the RRLs is shown in Fig. 11. The output current of  $g_{m\_HS}$  during two spinning phases is directly integrated by an auto-zeroed integrator. A comparator senses the polarity of the integrator's output, and increments or decrements the appropriate up/down counter (one for each RRL). The digital outputs of the three counters are then combined and applied to three DACs, which generate the appropriate compensation currents via  $g_m$  stages. According to the algorithm shown in Fig. 10, the offset components  $V_{os1}$  and  $V_{os2}$  are updated once in three spinning cycles.  $V_{os3}$  is updated twice every three spinning cycles, and will settle after  $V_{os1}$  and  $V_{os2}$  become sufficiently small. From (5) and (6), it should be noted that the contribution of  $V_{os1}$  and  $V_{os2}$  in the  $V_{os3}$  error signal

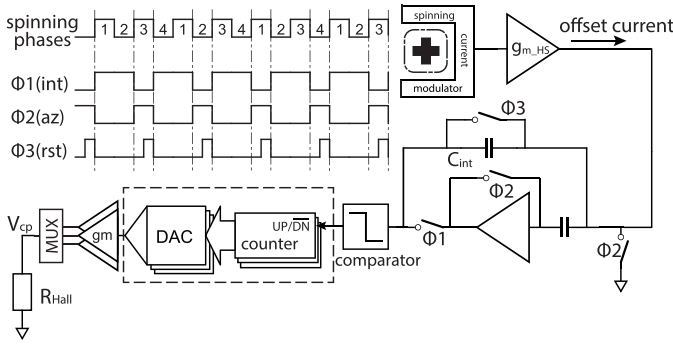


Fig. 11. Discrete-time implementation of the triple RRLs.

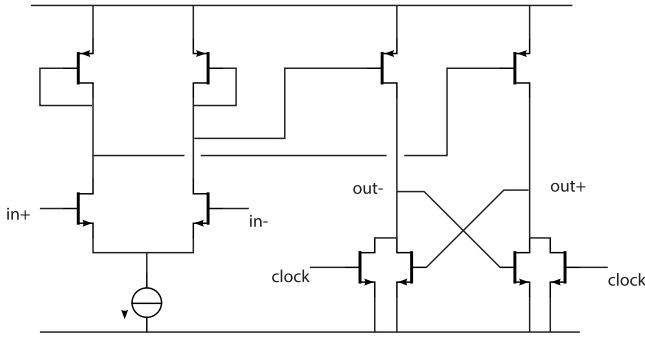


Fig. 12. Circuit diagram of the comparator.

appears with alternating polarity, and so  $V_{os3}$  will, on average, remain stable until the other two loops settle. At steady state, the residual offset  $V_{os1-3}$  will be limited to  $\pm 1$  LSB. The effectiveness of the discrete-time RRLs is similar to that of our previous implementation [18], [19]; however, its initial startup time is somewhat longer, about 360-ms worst case at an  $f_{spin}$  of 41.65 kHz.

Exploiting the auto-zeroing phase of the integrator, a discrete-time comparator is used, as shown in Fig. 12. Thanks to the large gain of the preceding integrator, its offset requirement is quite relaxed. With  $g_{m\_HS} = 1$ -mS, 10- $\mu$ s integration time and  $C_{int} = 20$  pF, a comparator offset of 1-mV results in a residual offset of 2  $\mu$ V at the Hall sensor outputs, which can be achieved with careful layout.

To avoid becoming stuck in local limit cycles, the DACs used in the RRLs need to be monotonic. For area efficiency and simplicity, the operation of the up/down counters and DACs is emulated by a multiplexed switched-capacitor (SC) integrator, as shown in Fig. 13. In  $\Phi 1$ , a reference voltage  $V_{ref}$  is sampled on a sampling capacitor  $C_s$ . During  $\Phi 2$ , depending on the comparator outputs, the charge stored on  $C_s$  is either added to or subtracted from one of three integration capacitors  $C_{os1-3}$ . The opamp in each integrator consists of a folded-cascode operational transconductance amplifier (OTA) and a pair of source followers to drive its common-mode feedback loop, as shown in Fig. 14. In this design,  $C_s = 150$  fF,  $C_{os1-3} = 10$  pF, and  $V_{ref} = 50$  mV result in a step-size of 0.75 mV. With a compensation  $g_m = 4$   $\mu$ S and  $R_{Hall} = 1$  k $\Omega$ , the residual ripple at the input of  $g_{m\_HS}$  can be reduced to 3  $\mu$ V. To maximize the input linear range of the feedback  $g_m$  stages, a 250-k $\Omega$  resistor is used to degenerate the input differential pair, as shown in Fig. 15.

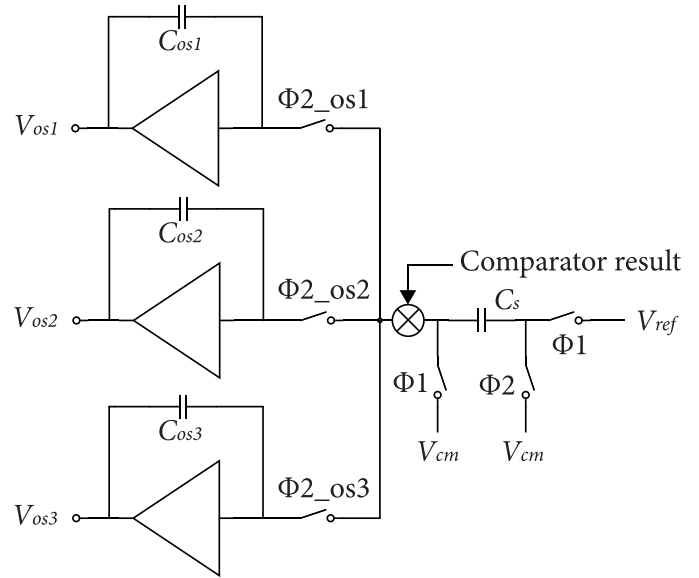


Fig. 13. SC integrator implementation of up/down counters and DACs.

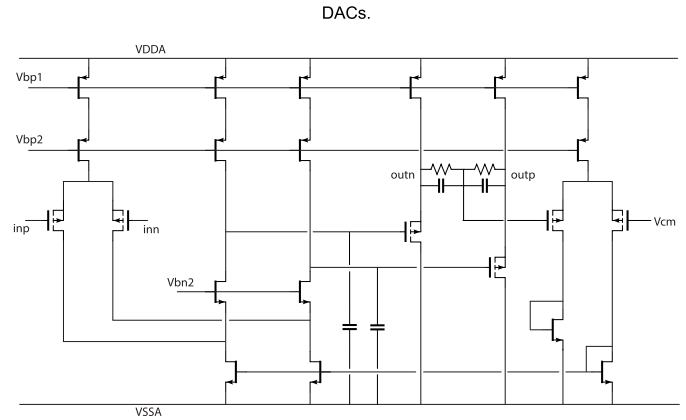
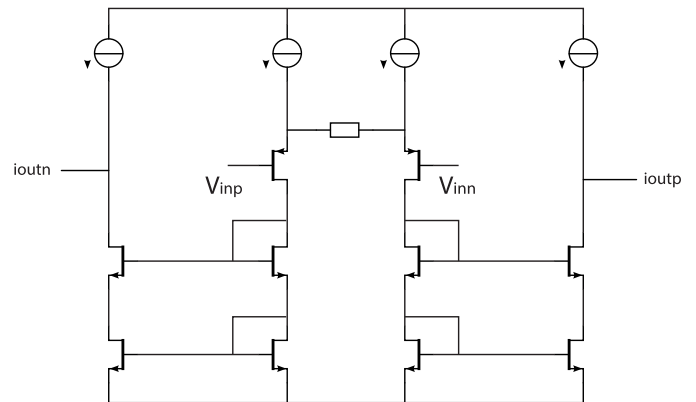


Fig. 14. Circuit diagram of the opamp used in the switch-cap integrators.

Fig. 15. Circuit diagram of the feedback  $g_m$  stage in RRLs.

To avoid voltage spikes due to compensation currents, the spinning Hall sensors are controlled by the two groups of clocks  $\phi_{1-4}$  and  $out_{1-4}$ , as shown in Fig. 16. During spinning phase transitions, clocks  $out_{1-4}$  briefly disconnect the Hall sensors and  $g_{m\_HS}$ , allowing the biasing current and



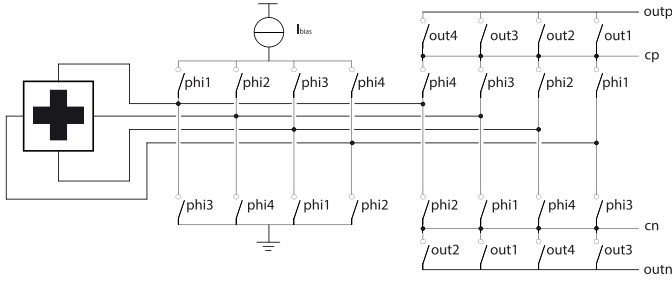


Fig. 16. Circuit diagram of the spinning current switches.

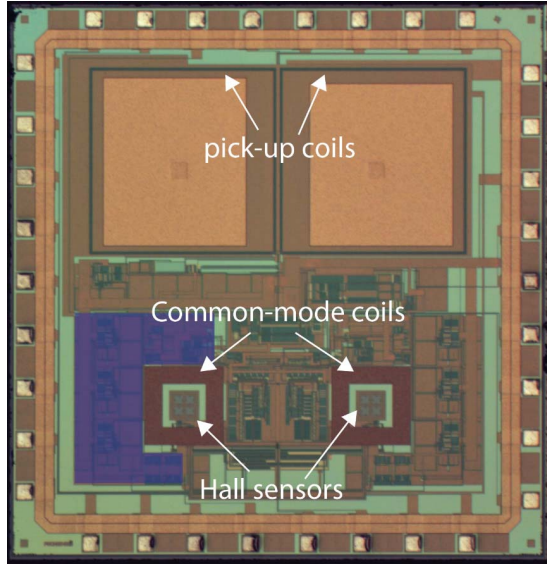


Fig. 17. Micro-chip photograph of the proposed system.

compensation current to settle. In this design, the dead band in out1–4 is set to 4 ns.

### III. EXPERIMENT RESULTS

The proposed system was fabricated in a  $0.18\text{-}\mu\text{m}$  CMOS process, and the chip photo is shown in Fig. 17. The total area is  $2.8\text{ mm} \times 2.9\text{ mm} = 8.12\text{ mm}^2$ . The pick-up coils in the HF path are built with metal traces, with a dimension of  $1\text{ mm} \times 2\text{ mm}$ . To avoid any HF crosstalk, the pick-up coils are placed away from the readout circuitry, and shielded by metal plates connected to ground. The common-mode coils for temperature stabilization are placed right on top of the Hall sensors, and have a measured resistance of  $220\ \Omega$ . The triple RRLs region for the left Hall sensor (highlighted in blue) occupies an area of about  $0.5\text{ mm}^2$ , which is about 20% smaller than our previous continuous-time implementation [18], [19].

To verify the performance of the triple RRLs, Fig. 18 shows the fast Fourier transform (FFT) of the system's output when the HF path is disabled. With  $f_{\text{spin}} = 41.65\text{ kHz}$  and zero magnetic field, the RRLs can reduce the spinning ripple from over  $1\text{ mT}$  down to  $21\ \mu\text{T}$  at  $83.3\text{ kHz}$  ( $2f_{\text{spin}}$ ). This residual ripple is limited by the mismatch between the current mirrors in the  $g_{m\text{-HS}}$  stage. At  $f_{\text{spin}} = 41.65\text{ kHz}$ , the residual ripple is reduced to  $2.9\ \mu\text{T}$ , which is solely limited by the step

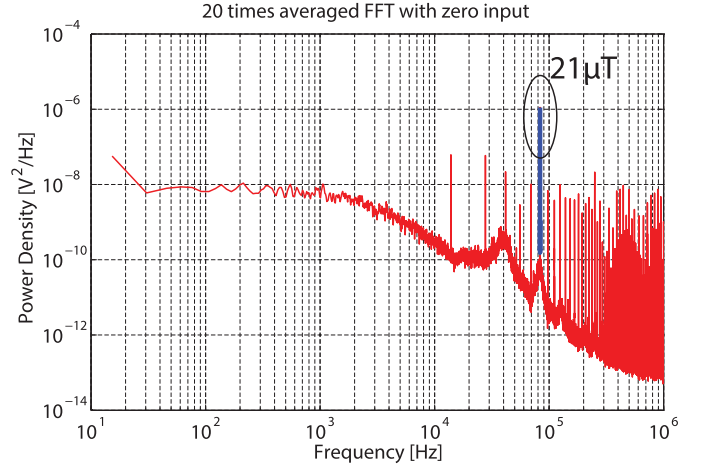


Fig. 18. FFT plot of system output with the HF path disabled and zero magnetic field.

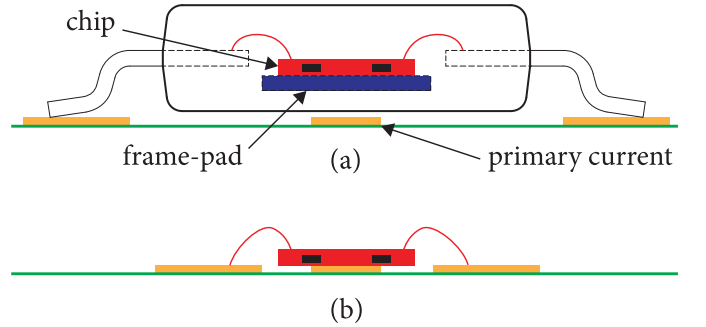


Fig. 19. Cross section of (a) traditional package and (b) COB.

size of the switched capacitor integrator in the RRLs. The residual ripple can be further reduced by increasing  $f_{\text{spin}}$ , at the expense of greater residual offset [17]. The sub-harmonics in the FFT plot are due to the fact that the modified RRL scheme is multiplexed between three ripple components, and it therefore under-samples the spinning ripple.

The lead-frame pads of traditional packages, as shown in Fig. 19(a), are known to generate eddy currents in response to HF magnetic fields, which, in turn, distort the sensor's HF response [20]. To avoid this, a chip-on-board (COB) technique is used to mount the die directly on the top of a PCB trace, with the added benefit of reducing the actual distance between the sensors and the primary current and their accurate alignment, as shown in Fig. 19(b). This results in a current-to-magnetic transfer function of about  $0.43\text{ mT/A}$ . After trimming at  $30\text{ }^\circ\text{C}$ , each Hall sensor is biased by a  $2\text{-mA}$  ( $0.5\text{ mA/plate}$ ) current, resulting in a sensitivity of about  $71.4\text{ mV/T}$ . With both LF and HF paths active, the system achieves a flat frequency response with a bandwidth of  $3\text{ MHz}$ , as shown in Fig. 20.

To accurately evaluate the proposed sensitivity stabilization scheme, a temperature-independent common-mode magnetic field reference is generated by feeding a square wave current with a constant amplitude into the on-chip common-mode coils. This is realized by placing the coils in the feedback of an off-chip inverting amplifier, which is driven by an  $80\text{-Hz}$  clock through an off-chip resistor, as shown in Fig. 21. In this design, the increase in coil resistance with

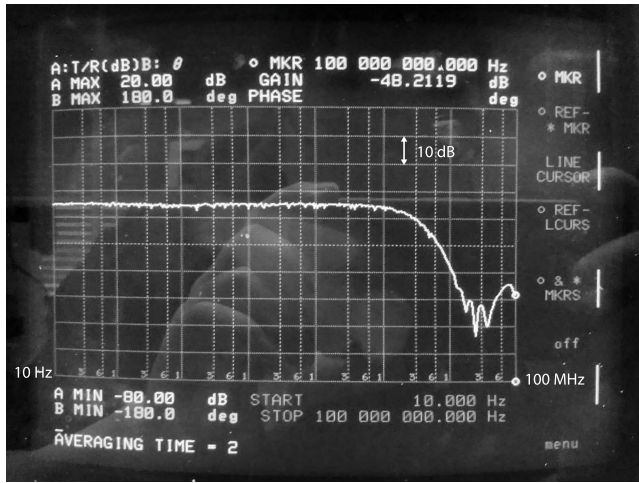


Fig. 20. Measured frequency response.

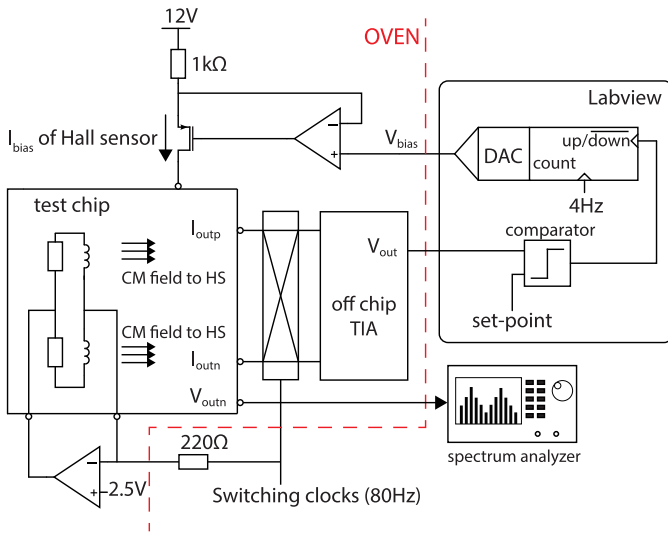


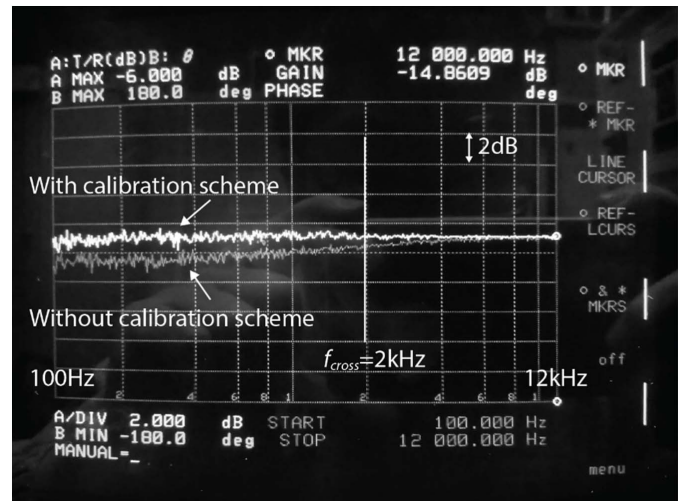
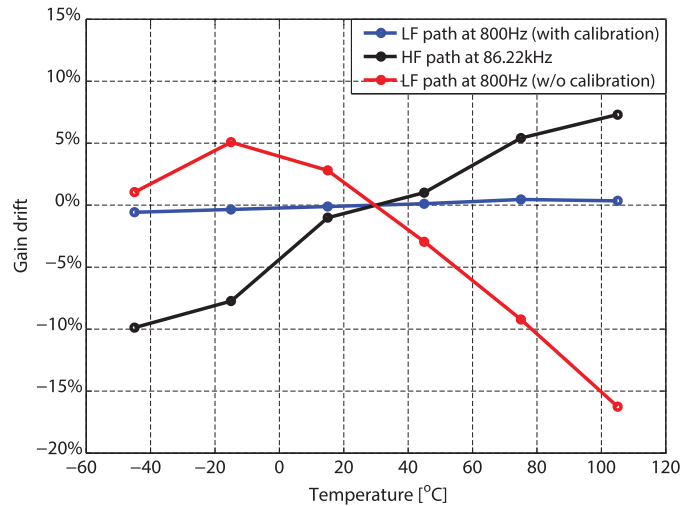
Fig. 21. Temperature stabilization test setup.

temperature limits the amplitude of the square wave current to  $\pm 10$  mA.

In principle, a reference current can be generated on-chip by combining a bandgap reference with the thin-film resistors available in the chosen process. With an accurate bandgap reference (see [26]), the effectiveness of the temperature stabilization will be preserved, as demonstrated by the negligible difference between the off-chip [21] and on-chip [27] realizations of a previous sensitivity stabilization scheme.

The output currents of the common-mode channel are synchronously demodulated, and read out by an off-chip TIA, whose averaged output voltages  $V_{out}$  are compared to a set-point by a comparator. The comparison results then increment or decrement a DAC by 1 LSB, which adjusts the Hall sensors' biasing current by  $5 \mu\text{A}$ .

Fig. 22 shows the measured system frequency response to  $3 \cdot A_{rms}$  currents at an ambient temperature of  $105^\circ\text{C}$  from 100 Hz to 12 kHz ( $f_{cross} = 2$  kHz). For these measurements, the temperature of the die was estimated to be about  $150^\circ\text{C}$ , mainly due to the heat dissipated in the relatively narrow (1 mm) PCB trace. Without the temperature

Fig. 22. Measured frequency response from 100 Hz to 12 kHz at  $105^\circ\text{C}$ .Fig. 23. Measured gain drift from  $-45^\circ\text{C}$  to  $105^\circ\text{C}$ .

stabilization scheme, a 2-dB gain mismatch can be observed across the frequency range. When activating the proposed stabilization scheme, this gain mismatch can be fully corrected. Up till 12 kHz, no gain mismatches can be observed between the HF and the stabilized LF paths.

The gain drift of the system is quantitatively characterized in an oven from  $-45^\circ\text{C}$  to  $105^\circ\text{C}$ . Driven by a spectrum analyzer, a primary current is generated outside the oven. The system outputs are directly analyzed by the same spectrum analyzer to extract the gains at the excitation frequencies. The measurement results are summarized in Fig. 23. Without sensitivity stabilization, the LF path gain at 800 Hz drifts as high as 22%, which is caused by the sensitivity drifts of both the Hall sensors and  $g_{m,HS}$ . With the proposed sensitivity stabilization scheme, the gain drift can be reduced to 1%, corresponding to a maximum temperature coefficient of  $76 \text{ ppm}/^\circ\text{C}$ , which is comparable to the state-of-the-art [21], [22].

Similarly, the sensitivity of the HF path is characterized at 86.22 kHz. The HF path gain drifts from  $-10\%$  to  $7\%$ , which was not observed in measurements up to 12 kHz (Fig. 22). This is because at HFs, the skin effect causes current crowding at

TABLE I  
COMPARISON TABLE

Source	This work		[20]	[21]	[25]
Technology	0.18 $\mu\text{m}$		0.35 $\mu\text{m}$	0.8 $\mu\text{m}$	N/A
Power supply	5 V		5 V	5 V	2.7 – 5.5 V
Supply current	9.2 mA*		12 mA	N/A	7 mA
Temperature compensation	Closed loop		Open loop	Closed loop	N/A
Sensitivity drift [ppm/°C]	76 (LF)	1100 (HF)	30	50	800**
Area [mm <sup>2</sup> ]	8.12		3.5	11.5	N/A
Input range	$\pm 7.8$ mT		$\pm 400$ -2.2 mT	$\pm 50$ mT	N/A
Bandwidth	3 MHz		125 kHz***	500 kHz****	50 kHz–1 MHz
Offset	80 $\mu\text{T}$		N/A	N/A	N/A

\* Off-chip components not included

\*\* >20% full scale input

\*\*\* Calculated based on spinning frequency

\*\*\*\* Theoretical value

the surface of the conductor. This, in turn, increases the trace's impedance and its temperature, thus reducing the amplitude of the primary current flowing through the shunt resistors. In addition, the HF magnetic field will interact with its surrounding components. The permeability of some of these will be temperature dependent, therefore influencing the current-to-magnetic field transfer of the primary current. Together with the non-linearity of  $g_{m\_coil}$  due to the large coil voltage swing, this may result in additional sensitivity drift. Nevertheless, the sensitivity of the HF path is comparable to the performance of other coil-based magnetic sensors [28].

Table I summarizes the performance of this design in comparison to other state-of-the-art CMOS low-drift magnetic sensors. Compared to low-drift Hall sensors with other temperature stabilization schemes, the proposed scheme achieves comparable gain accuracy as [21] and [22], while the bandwidth is at least  $6\times$  higher. Compared to other coil-based magnetic sensors like [28], the proposed system can cover the full bandwidth including dc while achieving similar gain accuracy.

#### IV. CONCLUSION

This paper presents a hybrid magnetic sensor built of Hall sensors and pick-up coils with its Hall sensor gain drift continuously stabilized. The proposed sensitivity stabilization scheme exploits the common-mode rejection of differential current sensing systems by injecting an ac common-mode magnetic field reference, through which the system sensitivity can be actively monitored and hence, stabilized. With this approach, the overall Hall sensitivity drift can be reduced from 22% to 1% in the temperature range from  $-45$  °C to  $105$  °C. This is equivalent to a temperature coefficient of 76 ppm/°C.

Furthermore, the triple RRLs for spinning current Hall sensors are implemented in a discrete-time manner, which occupies 20% less chip area compared to the previous continuous-time implementation. By combining the sensitivity stabilized Hall sensors and the temperature-independent pick-up coil, the overall system achieves a flat bandwidth from dc to 3 MHz.

#### ACKNOWLEDGMENT

The authors would like to thank Texas Instruments for chip fabrication.

#### REFERENCES

- [1] S. H. Shalmany, D. Draxelmayr, and K. A. A. Makinwa, "A  $\pm 5$  A integrated current-sensing system with  $\pm 0.3\%$  gain error and 16  $\mu\text{A}$  offset from  $-55$  °C to  $+85$  °C," *IEEE J. Solid-State Circuits*, vol. 51, no. 4, pp. 800–808, Apr. 2016.
- [2] C. Xiao, L. Zhao, T. Asada, W. G. Odendaal, and J. D. van Wyk, "An overview of integratable current sensor technologies," in *Proc. IAS Annu. Meeting*, vol. 2, 2003, pp. 1251–1258.
- [3] M. K. Alghamdi and A. A. Hamoui, "A spurious-free switching buck converter achieving enhanced light-load efficiency by using a  $\Delta\Sigma$ -modulator controller with a scalable sampling frequency," *IEEE J. Solid-State Circuits*, vol. 47, no. 4, pp. 841–851, Apr. 2012.
- [4] S.-W. Hong *et al.*, "High area-efficient DC-DC converter with high reliability using time-mode Miller compensation (TMMC)," *IEEE J. Solid-State Circuits*, vol. 48, no. 10, pp. 2457–2468, Oct. 2013.
- [5] B. Miedzinski, A. Szymanski, W. Dzierzanowski, and B. Wojszczyk, "Performance of Hall sensors when used in ground fault protections in MV networks," in *Proc. Conf. Univ. Power Eng. (UPEC)*, Sep. 2004, pp. 753–757.
- [6] A. Elez, S. Car, and Z. Maljković, "Detection of inter-coil short circuits in synchronous machine armature winding on the basis of analysis of machine magnetic field," in *Proc. Int. 19th Elect. Mach. (ICEM)*, Sep. 2010, pp. 1–6.
- [7] R. S. Popovic, *Hall Effect Devices*. Boca Raton, FL, USA: CRC Press, 2003.
- [8] L. M. Stephenson and H. E. M. Barlow, "Power measurement at 4 Gc/s by the application of the Hall effect in a semiconductor," *Proc. IEE—Part B, Radio Electron. Eng.*, vol. 106, no. 25, pp. 27–30, Jan. 1959.



- [9] P. Ripka and M. Janosek, "Advances in magnetic field sensors," *IEEE Sensors J.*, vol. 10, no. 6, pp. 1108–1116, Jun. 2010.
- [10] G. Boero, M. Demierre, P.-A. Besse, and R. Popovic, "Micro-Hall devices: Performance, technologies and applications," *Sens. Actuators A: Phys.*, vol. 106, pp. 314–320, Sep. 2003.
- [11] R. T. Merrill, M. W. McElhinny, and P. L. McFadden, *Magnetic Field of the Earth*, vol. 63. San Diego, CA, USA: Academic, 1996.
- [12] P. Munter, "A low-offset spinning-current Hall plate," *Sens. Actuators A: Phys.*, vol. 22, pp. 743–746, Jun. 1989.
- [13] O. Paul, P. Ruther, L. Plattner, and H. Baltes, "A thermal van der Pauw test structure," *IEEE Trans. Semicond. Manuf.*, vol. 13, no. 2, pp. 159–166, May 2000.
- [14] M. Motz *et al.*, "A miniature digital current sensor with differential Hall probes using enhanced chopping techniques and mechanical stress compensation," in *Proc. IEEE SENSORS*, Oct. 2012, pp. 1–4.
- [15] J. C. van der Meer, F. R. Riedijk, E. van Kampen, K. A. A. Makinwa, and J. H. Huijsing, "A fully integrated CMOS Hall sensor with a  $3.65 \mu\text{T}$   $3\sigma$  offset for compass applications," in *IEEE Int. Solid-State Circuits Conf. (ISSCC) Dig. Tech. Papers*, Feb. 2005, pp. 246–247.
- [16] P. D. Dimitropoulos, P. M. Drljaca, and R. S. Popovic, "A  $0.35 \mu\text{m}$ -CMOS, wide-band, low-noise Hall magnetometer for current sensing applications," in *Proc. IEEE Sensors*, Oct. 2007, pp. 884–887.
- [17] J. Jiang, W. Kindt, and K. A. A. Makinwa, "A continuous-time ripple reduction technique for spinning-current Hall sensors," *IEEE J. Solid-State Circuits*, vol. 49, no. 7, pp. 1525–1534, Jul. 2014.
- [18] J. Jiang and K. Makinwa, "A multi-path CMOS Hall sensor with integrated ripple reduction loops," in *Proc. Conf. ASSCC*, Nov. 2015, pp. 53–56.
- [19] J. Jiang and K. Makinwa, "A hybrid multipath CMOS magnetic sensor with  $210 \mu\text{T}$  resolution and 3MHz bandwidth for contactless current sensing," in *IEEE Int. Solid-State Circuits Conf. (ISSCC) Dig. Tech. Papers*, Feb. 2016, pp. 204–205.
- [20] J. Jiang and K. Makinwa, "Multi-path wide-bandwidth CMOS magnetic sensors," *IEEE J. Solid-State Circuits*, vol. 52, no. 1, pp. 198–209, Jan. 2017.
- [21] S. Huber, W. Leten, M. Ackermann, C. Schott, and O. Paul, "A fully integrated analog compensation for the Piezo-Hall effect in a CMOS single-chip Hall sensor microsystem," *IEEE Sensors J.*, vol. 15, no. 5, pp. 2924–2933, May 2015.
- [22] M. Pastre, M. Kayal, and H. Blanchard, "A Hall sensor analog front end for current measurement with continuous gain calibration," *IEEE Sensors J.*, vol. 7, no. 5, pp. 860–867, May 2007.
- [23] J. Maupin and M. Geske, "The Hall effect in silicon circuits," in *The Hall Effect its Applications*. New York, NY, USA: Springer, 1980, pp. 421–445.
- [24] J. Jiang and K. Makinwa, "A hybrid multi-path CMOS magnetic sensor with  $76 \text{ ppm}/^\circ\text{C}$  sensitivity drift," in *Proc. Conf. ESSCIRC*, Sep. 2016, pp. 397–400.
- [25] R. Wu, J. H. Huijsing, and K. A. A. Makinwa, "A current-feedback instrumentation amplifier with a gain error reduction loop and 0.06% untrimmed gain error," *IEEE J. Solid-State Circuits*, vol. 46, no. 12, pp. 2794–2806, Dec. 2011.
- [26] G. Maderbacher *et al.*, "A digitally assisted single-point-calibration CMOS bandgap voltage reference with a  $3\sigma$  inaccuracy of  $\pm 0.08\%$  for fuel-gauge applications," in *IEEE Int. Solid-State Circuits Conf. (ISSCC) Dig. Tech. Papers*, Feb. 2015, pp. 102–104.
- [27] A. Ajbl, M. Pastre, and M. Kayal, "A fully integrated Hall sensor microsystem for contactless current measurement," *IEEE Sensors J.*, vol. 13, no. 6, pp. 2271–2278, Jun. 2013.
- [28] Si850x/1x, Silicon Labs, accessed on Jan. 2016. [Online]. Available: <http://www.silabs.com/documents/public/pcns/EOL-1601111-Si850x-1x-Product-Family.pdf>



**Junfeng Jiang** received the B.Sc. degree from the Dalian University of Technology, Dalian, China, in 2009, and the M.Sc. degree from the Delft University of Technology, Delft, The Netherlands, in 2011, where he has been pursuing the Ph.D. degree since 2011 in the Electronic Instrumentation Laboratory, with a focus on the design of a wide-bandwidth contact-less current sensor.

He is currently an Analog Designer with Texas Instruments, Freising, Germany.

Mr. Jiang was a recipient of the SSCS Predoctoral Achievement Award in 2016 and 2017, and the ASSCC Student Travel Grant in 2015.



**Kofi A. A. Makinwa** (M'97–SM'05–F'11) received the B.Sc. and M.Sc. degrees from Obafemi Awolowo University, Ile-Ife, Nigeria, in 1985 and 1988, respectively, the M.E.E. degree from the Philips International Institute, Eindhoven, The Netherlands, in 1989, and the Ph.D. degree from the Delft University of Technology, Delft, The Netherlands, in 2004.

From 1989 to 1999, he was a Research Scientist with the Philips Research Laboratories, Eindhoven, where he was involved in the interactive displays and digital recording systems. In 1999, he joined the Delft University of Technology, where he is currently an Antoni van Leeuwenhoek Professor and the Head of the Microelectronics Department. He has authored ten books and over 200 technical papers, and holds 25 patents. His current research interests include the design of precision mixed-signal circuits, sigma-delta modulators, smart sensors, and sensor interfaces.

Dr. Makinwa was awarded the 2005 Simon Stevin Gezel Award from the Dutch Technology Foundation, for his doctoral research. He was a co-recipient of several best paper awards from the IEEE JOURNAL OF SOLID-STATE CIRCUITS (JSSC), the International Solid-State Circuits Conference (ISSCC), Transducers, and the European Solid-State Circuits Conference (ESSCIRC). He is an alumnus of the Young Academy of the Royal Netherlands Academy of Arts and Sciences and an elected Member of the IEEE Solid-State Circuits Society AdCom, the society's governing board. He is the Analog Subcommittee Chair of ISSCC. He also serves on the program committees of the VLSI Symposium, ESSCIRC, and the Advances in Analog Circuit Design workshop. He is a Guest Editor of JSSC and a Distinguished Lecturer of the IEEE Solid-State Circuits Society.